INTERNATIONAL JOURNAL FOR NUMERICAL METHODS IN BIOMEDICAL ENGINEERING
Int. J. Numer. Meth. Biomed. Engng. 2010; **26**:511–523
Published online 12 March 2009 in Wiley InterScience (www.interscience.wiley.com). DOI: 10.1002/cnm.1242

Overlap domain decomposition method for bioluminescence tomography (BLT)

Tao Wang[1,2], Shuping Gao[1,2], Ling Zhang[1,2], Yan Wu[2], Xiaowei He[2], Yanbin Hou[2], Heyu Huang[2] and Jie Tian[2,3,*,†]

[1]*Department of Applied Mathematics, Xidian University, Xi'an, Shaanxi 710071, China*
[2]*Life Science Research Center, Xidian University, Xi'an, Shaanxi 710071, China*
[3]*Medical Image Processing Group, Institute of Automation, Chinese Academy of Sciences, Beijing 100080, People's Republic of China*

SUMMARY

Bioluminescence tomography (BLT) allows *in vivo* localization and quantification of bioluminescent sources inside a small animal to reveal various molecular and cellular activities. In this paper, the overlap domain decomposition method (ODDM) of BLT is proposed, which refers to divide and conquer techniques for solving BLT by iteratively solving sub-problems on smaller sub-domains. Here, two triangulations of the region are adopted. We can obtain the photon density distribution on the object surface, as well as reconstruct the position of the light source by using ODDM and genetic algorithm. The numerical simulations have shown that ODDM is computationally efficient and fairly robust. Copyright © 2009 John Wiley & Sons, Ltd.

Received 30 March 2008; Revised 2 February 2009; Accepted 3 February 2009

KEY WORDS: tomography; image reconstruction techniques; overlap domain decomposition method; finite element method; symmetric positive definite matrix

1. INTRODUCTION

Molecular imaging is a newly emerging field in which the modern tools of molecular and cell biology are being married to state-of-art technology for noninvasive imaging [1]. Recently, the small-animal molecular imaging is a rapidly developing biomedical imaging field. The goals of this field are to develop technologies and assays for imaging molecular events in living organisms. Bioluminescence tomography (BLT) is a promising medical imaging modality using near infrared spectroscopy to ascertain the position of the light source.

For performance evaluation of BLT algorithms, the simulation of photon transportation in the biologic tissues plays an important role [2, 3]. A popular approach of photon propagation modeling

*Correspondence to: Jie Tian, Medical Image Processing Group, Institute of Automation, Chinese Academy of Sciences, Beijing 100080, People's Republic of China.
†E-mail: tian@ieee.org

Contract/grant sponsor: National Basic Research Program of China (NBRPC); contract/grant number: 2006CB705700
Contract/grant sponsor: Program for Cheung Kong Scholars and Innovative Research Team in University (PCSIRT); contract/grant number: IRT0645
Contract/grant sponsor: Chair Professors of Cheung Kong Scholars Programme
Contract/grant sponsor: Shaanxi Science and Technology Programming; contract/grant number: 2007K08-06

in highly scattering media is the diffusion equation derived from simplified assumptions applied to RTE [4]. The numerical method is preferred when dealing with complex geometries [5–7] such as the finite element method (FEM), boundary integral method and multi-spectral bioluminescence optical tomography.

Because the computation complexity of photon density and source density increases quickly with the number of dimensions and nodes, real-time computation of BLT needs to reduce the complexity of the problem. In this paper, we present the overlap domain decomposition method (ODDM) for BLT. The outstanding advantage of ODDM is to distribute parallel numerical solvers on smaller sub-domains and make the computation extremely efficient. The two-level additive Schwarz method is developed to solve the forward problem of BLT. The emphasis of this paper is to apply the idea of two-level domain decomposition to optimize the source density of the BLT inverse problem. It is shown that the two-level approaches are indispensable in the algorithm due to the properties of local convergence results. For BLT inverse problem, after the photon density is obtained by ODDM, the genetic algorithm is employed to reconstruct the position of the source. Numerical simulations illustrate that ODDM is more feasible and effective than FEM.

The paper is organized as follows: in Section 2, the forward solver based on photon diffusion equation model is described. In Section 3, ODDM applies domain decomposition techniques for the forward and inverse problems of BLT. The convergence of the additive Schwarz method is proved. In Section 4, the numerical simulations are shown and conclusions are drawn.

2. DIFFUSION EQUATION

When the bioluminescence imaging experiment is carried out in a dark environment, the propagation of bioluminescent photons into biological tissue can be modeled by the steady-state diffusion equation and Robin boundary condition [4, 8]:

$$\begin{aligned} L\Phi &= -\nabla\cdot(D(x)\nabla\Phi(x)+\mu_a(x)\Phi(x)) = S(x) \quad (x\in\Omega) \\ \Phi(x)&+2A(x)D(x)(v(x)\cdot\nabla\Phi(x)) = 0 \quad (x\in\partial\Omega) \end{aligned} \tag{1}$$

where Ω and $\partial\Omega$ are the domain and its boundary, respectively; $\Phi(x)$ denotes the photon flux density (W/mm^3); $S(x)$ is the source energy density (W/mm^3); $\mu_\alpha(x)$ is the absorption coefficient (mm^{-1}); $D(x)=1/(3(\mu_\alpha(x)+(1-g)\mu_s(x)))$ is the optical diffusion coefficient (mm), $\mu_s(x)$ is the scattering coefficient (mm^{-1}) and g is the anisotropy parameter; and v is the unit outer normal on $\partial\Omega$. Given the mismatch between the refractive indices n for Ω and n' for the external medium, $A(x;n,n')$ can be approximately represented as

$$A(X;n,n')=\frac{1+R(x)}{1-R(x)}$$

where $R(x)$ can be approximated by $R(x)\approx -1.4399n^{-2}+0.7099n^{-1}+0.6681+0.0636n$ [9]. The measured quantity is the outgoing flux density $Q(x)$ on $\partial\Omega$, which is

$$Q(x)=-D(x)(v\cdot\nabla\Phi(x))=\frac{\Phi(x)}{2A(x;n,n')}(x\in\partial\Omega)$$

BLT is used to reconstruct the bioluminescent source distribution inside an object based on the photon flux measured at its boundary. However, BLT problem is ill-posed in theory and its solution is not unique without sufficient *a priori* knowledge. Thus, the solution to Equation (1) is focus for BLT.

DOI: 10.1002/cnm

3. OVERLAPPING DECOMPOSITION DOMAIN METHOD

3.1. Weak-form equation

Based on the principle of virtual work, the weak solution of the photon flux density $\Phi(x)$ is given through Equation (1):

$$\int_\Omega D(x)(\nabla\Phi(x))\cdot(\nabla\Psi(x))\,dx+\int_\Omega \mu_a(x)\Phi(x)\Psi(x)\,dx+\int_{\partial\Omega}\frac{1}{2A_n(x)}\Phi(x)\Psi(x)\,dx$$
$$=\int_\Omega S(x)\Psi(x)\,dx \quad (\forall\Psi(x)\in H^1(\Omega)) \tag{2}$$

Here $H^1(\Omega)$ is the Sobolev space. Then Equation (2) can be written as

$$\alpha(\Phi,\Psi)=F(\Psi) \tag{3}$$

where,

$$\alpha(\Phi,\Psi)=\int_\Omega D(x)(\nabla\Phi(x))\cdot(\nabla\Psi(x))\,dx+\int_\Omega \mu_\alpha(x)\Phi(x)\Psi(x)\,dx+\int_{\partial\Omega}\frac{1}{2A_n(x)}\Phi(x)\Psi(x)\,dx$$
$$F(\Psi)=\int_\Omega S(x)\Psi(x)\,dx$$

We are particularly interested in the solution of Equation (3) discretization (by either finite element method or finite difference method), which yields a large sparse, symmetric positive definite linear system: $M\Phi=F$.

Considering the approximation Φ^h of the exact solution Φ and the uniqueness of the BLT problem solution, the following error bound was derived [10, 11]:

$$\|\Phi(S_\lambda)-\Phi^h(S_\lambda^h)\|^2_{L^2(\Omega)}+\sqrt{\lambda}\|S_\lambda-S_\lambda^h\|^2_{L^2(\Omega)}\leqslant ch^{3/4} \tag{4}$$

where $\Phi(S_\lambda)\in H^1(\Omega)$, $S_\lambda\in L^2(\Omega)$. $\Phi^h(S_\lambda^h)$ and S_λ^h correspond to $\Phi(S_\lambda)$ and S_λ, which are obtained by introducing a regular triangulation Λ_h of Ω and finite element space V_h; λ is the regularization parameter; h denotes the maximum element size of the triangulation and c is a constant independent of λ and h. Based on Equation (4), it is a beneficial improvement for the BLT solution to reduce the maximum element size h.

3.2. ODDM for inverse problem

Overlapping domain decomposition algorithms are based on a decomposition of the domain Ω into a number of overlapping sub-regions. Here, we consider the case of the two overlapping sub-regions $\{\Omega_1,\Omega_2\}$ that form a covering of Ω; see Figure 1. Let $\Gamma_i, i=1,2$, denote the part of the boundary of Ω_i that is in the interior of Ω.

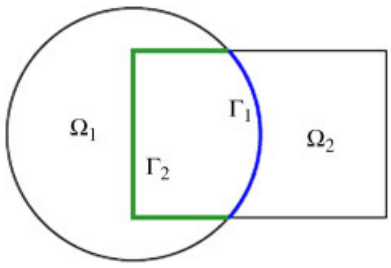

Figure 1. Two sub-domain decompositions.

DOI: 10.1002/cnm

The basic Schwarz alternating algorithm to solve Equation (1) starts with any suitable initial guess Φ^0 and constructs a sequence of improved approximation of $\Phi^1, \Phi^2, \ldots$. Starting with the iteration sequence Φ^k, we solve the following two sub-problems Ω_1 and Ω_2 successively with the most current values used as a boundary condition on the artificial interior boundaries:

$$L\Phi_1^{k+1} = f \quad \text{on } \Omega_1$$
$$\Phi_1^{k+1} = \Phi^k \quad \text{on } \Gamma_1$$
$$2AD\frac{\partial \Phi_1^{k+1}}{\partial v} - \Phi_1^{k+1} = 0 \quad \text{on } \partial\Omega_1/\Gamma_1$$

and

$$L\Phi_2^{k+1} = f \quad \text{on } \Omega_2$$
$$\Phi_2^{k+1} = \Phi_1^{k} \quad \text{on } \Gamma_2$$
$$2AD\frac{\partial \Phi_2^{k+1}}{\partial v} - \Phi_2^{k+1} = 0 \quad \text{on } \partial\Omega_2/\Gamma_2$$

The iteration sequence Φ^{k+1} is defined by

$$\Phi^{k+1}(X) = \begin{cases} \Phi_2^{k+1} & \text{if } X \in \Omega_2 \\ \Phi_1^{k+1} & \text{if } X \in \Omega/\Omega_2 \end{cases}$$

It is shown that in the norm induced by operator L, the iteration $\{\Phi^k\}$ converges geometrically to Φ on Ω [12].

The above Schwarz procedure extends almost verbatim to discretions of Equation (1). We describe the algorithm in matrix notation. Corresponding to the sub-regions $\{\Omega_1, \Omega_2\}$, let $\{I_1, I_2\}$ denote the indices of the nodes in the interior of Ω_1 and Ω_2, respectively. Thus, I_1 and I_2 form an overlap set of indices for the unknown vector Φ. Let n_1 and n_2 be the number of indices in I_1 and I_2, respectively. Owing to overlap, $n_1 + n_2 > n$, where n is the number of unknowns in Ω.

Corresponding to each Ω_i, we define a rectangular $n \times n_i$ extension matrix R_i^{T} [13] whose action extends by zeros to a vector of nodal values in Ω_i. Thus, given a sub-vector x_i of length n_i with nodal values at the interior nodes on Ω_i, we define

$$(R_i^{\mathrm{T}} x_i) = \begin{cases} (x_i)_k & \text{for } k \in I_i \\ 0 & \text{for } k \in I - I_i \text{ where } I = I_1 \cup I_2 \end{cases}$$

The transposed matrix R_i of this extension map R_i^{T} is a restriction matrix whose action restricts a full vector x of length n to a vector size n_i by choosing the entries with indices I_i corresponding to the interior nodal in Ω_i. As a result, $R_i x$ is the sub-vector of nodal values of x in the interior of Ω_i. The local sub-domain matrices (corresponding to the discretion on Ω_i) are, therefore, $M_1 = R_1 M R_1^{\mathrm{T}}$, $M_2 = R_2 M R_2^{\mathrm{T}}$ and these are principle sub-matrices of M.

The discrete version of the Schwarz alternating method (described above) solves $M\Phi = F$, and starts with any suitable initial guess Φ^0, generating a sequence that iterates $\Phi^0, \Phi^1, \ldots$ as follows:

$$\Phi^{k+1/2} = \Phi^k + R_1^{\mathrm{T}} M_1^{-1} R_1 (F - M\Phi^k) \tag{5}$$

$$\Phi^{k+1} = \Phi^{k+1/2} + R_2^{\mathrm{T}} M_2^{-1} R_2 (F - M\Phi^{k+1/2}) \tag{6}$$

Note that this corresponds to a generalization of the block Gauss–Seidal iteration (with overlapping blocks) for solving Equation (1). At each iteration, two sub-domain solvers are required. Defining $P_i = R_i^{\mathrm{T}} M_i^{-1} R_i M$, $i = 1, 2$.

The convergence is governed by the iteration matrix $(I - P_2)(I - P_1)$, which is often called a multiplicative Schwarz iteration. With sufficient overlap, it can be proved that the above algorithm is convergent with a rate independent of mesh size h [13].

DOI: 10.1002/cnm

We note that P_1 and P_2 are symmetrical with respect to the M inner product, but not so for the iteration matrix $(I-P_2)(I-P_1)$. A symmetrical version can be constructed by iterating one more half-step with M_1^{-1} after Equation (6). The resulting iteration matrix becomes $(I-P_1)(I-P_2)(I-P_1)$, which is symmetrical with respect to M inner product; therefore, conjugate gradient acceleration can also be applied.

An analogous block Jacobi version can be also defined as

$$\Phi^{k+1/2} = \Phi^k + R_1^{\mathrm{T}} M_1^{-1} R_1 (F - M\Phi^k)$$

$$\Phi^{k+1} = \Phi^{k+1/2} + R_2^{\mathrm{T}} M_2^{-1} R_2 (F - M\Phi^k)$$

This version is more parallelizable because the two sub-domain solvers can be carried out concurrently. By eliminating $\Phi^{k+1/2}$, we obtain

$$\Phi^{k+1} = \Phi^k + (R_1^{\mathrm{T}} M_1^{-1} R_1 + R_2^{\mathrm{T}} M_2^{-1} R_2)(F - M\Phi^k)$$

This is simply the Richardson iteration on $M\Phi = F$ with the following additive Schwarz preconditioner for $M: A^{-1} = R_1^{\mathrm{T}} M_1^{-1} R_1 + R_2^{\mathrm{T}} M_2^{-1} R_2$; the preconditioned system can be written as $A^{-1}M = P_1 + P_2$, which is symmetrical with respect to the M inner product [13] and can also be used with conjugate gradient acceleration. Again, for suitably chosen overlap, the condition number of the preconditioned system is bound independently of h (unlike classical block Jacobi).

We can compute Equation (3) by an FEM. For simplicity, we consider only continuous, piecewise linear, tetrahedral elements in R^3. In order to get photon density from the surface of the object, a commonly used method for computing photon densities via FEM is used. In addition, we apply the ODDM to Equation (3) in order to reduce computation complexity of the problem.

The shape of photon density has a peak around the source and decreases rapidly far from the source. Thus, adding the Schwarz method to one level is not sufficient, since the domain is far from the sources; it may neglect the existence of sources, especially in the case where there are multiple sub-domains. As a result, we must refine the mesh and adopt two-level ODDM.

To define our algorithms, we need two levels of triangulation that have already been introduced in [13, 14]. Let $\Omega \in R^3$ be a polygonal domain with boundary $\partial\Omega$ and $\alpha(\Phi, \Psi) = (\Phi, \Psi)_{L^2(\Omega)}$. Here, $\Phi, \Psi \in V_h$ and V_h are the usual triangular finite element subspaces of $H^1(\Omega)$, consisting of a continuous piecewise liner function. Following the Dryja–Widlund construction of the overlapping decomposition of V_h, the triangulation of Ω is introduced as follows.The region is first divided into non-overlapping sub-structures Ω_k and $(k = 1, 2, \ldots, N)$, whose union forms a coarse subdivision of Ω. Then, all the sub-structures Ω_k, which have a diameter of order H, are divided into elements of size h. The assumption, common in finite element theory, is that all elements are regularly shaped. To obtain an overlapping decomposition of the domain, we extend each sub-region Ω_k to a larger region Ω_k', consisting of all points Ω within a distance of βH from Ω_k whose range is from 0 to 1 i.e. $\Omega_k \subset \Omega_k'$. We assume that the overlap is uniform and $V_k \subset V_h$ is the usual finite element space over Ω_i'. Let $V_0 \subset V_h$ be a triangular finite element subspace defined on the coarse grid. It is clear that $\Omega = \bigcup_k \Omega_k'$ and $V_h = V_0 + \cdots + V_N$.

Based on the decomposition of V_h discussed above, which includes N elements and N_k vertex nodes, we introduce and analyze some algorithms for the finite element solution of the expression equation (3). Let $\{\psi_1, \psi_2, \ldots, \psi_{N_k}\}$ be the nodal basis of the space V_h and $\Phi_k(x)$ is an approximation of $\Phi(x)$:

$$\Phi_k(x) = \sum_{i=1}^{N_k} \phi_i(x)\psi_i(x) \tag{7}$$

$$\Psi_k(x) = \sum_{i=1}^{N_k} \varphi_i(x)\psi_i(x) \tag{8}$$

DOI: 10.1002/cnm

where $\phi_i(x)$, $\varphi_i(x)$ is the ith node value. Incorporating Equations (7) and (8) in Equation (3), we have

$$\alpha(\Phi_k(x), \Psi_k(x)) = F(\Psi_k(x)) \tag{9}$$

or

$$\sum_{j=1}^{N_k} \alpha(\psi_i(x), \psi_j(x))\Phi_j = F(\psi_j(x))$$

Equation (9) is a linear algebraic equation, noted as $M\Phi = f$, where

$$M = \begin{pmatrix} \alpha(\psi_1, \psi_1) & \cdots & \alpha(\psi_{N_k}, \psi_1) \\ \vdots & \ddots & \vdots \\ \alpha(\psi_1, \psi_{N_k}) & \cdots & \alpha(\psi_{N_k}, \psi_{N_k}) \end{pmatrix}, \quad \Phi = \begin{pmatrix} \Phi_1^k \\ \vdots \\ \Phi_{N_k}^k \end{pmatrix}, \quad f = \begin{pmatrix} F(\psi_1) \\ \vdots \\ F(\psi_{N_k}) \end{pmatrix}$$

Let $B(\Phi) = \alpha(\Phi_k(x), \Psi_k(x))$, $f_k = F(\Psi_k(x))$, then we have

$$G(\Phi) = B(\Phi) - f_k = 0 \tag{10}$$

For each sub-space V_i, let us define an operator $Q_k : V_h \to V_k$, by $b(Q_k(\Phi), \Psi) = \alpha(\Phi, \Psi)$ (where $b(\cdot, \cdot)$ is a Poisson operator, which generally has nothing to do with the non linear problem to be solved). $\forall \Phi \in V_h, \Psi \in V_k$, $Q_k(\Phi)$ can also be understood in the matrix form, $Q_k(u) = R_k^{\mathrm{T}} M_k^{-1} R_k B(\Phi)$, where M_k is the sub-domain discretion of $b(Q_k(\Phi), \Psi)$ and $R_k : V_h \to V_k$ is a restriction operator [12]. To define the additive Schwarz method, let us characterize $Q = Q_0 + Q_1 + \cdots + Q_N$. We note that the operators Q_k and Q are generally not linear as shown in the following non-linear equation:

$$\tilde{G}(\Phi) = Q(\Phi) - \tilde{g} = 0$$

which is equivalent to Equation (10), since they both have the same solution. For a properly chosen parameter λ, iterative for $k = 0, 1, \ldots$ until convergence of

$$\Phi^{k+1} = \Phi^k + \lambda S^k \tag{11}$$

where $S^k = -\tilde{G}(\Phi^k)$. Then Equation (11) can be expressed as

$$\begin{aligned} \Phi^{k+1} &= \Phi^k + \lambda \sum_{i=1}^{p} R_i^{\mathrm{T}} M_i^{-1} R_i (F - M\Phi^k) \\ &= \left(I - \lambda \sum_{i=1}^{p} R_i^{\mathrm{T}} M_i^{-1} R_i M \right) \Phi^k + \left(\lambda \sum_{i=1}^{p} R_i^{\mathrm{T}} M_i^{-1} R_i \right) F \\ &= T_{as} \Phi^k + A_{as}^{-1} F \end{aligned} \tag{12}$$

where $T_{as} = I - A_{as}^{-1} M$, $A_{as}^{-1} = \lambda \sum_{i=1}^{p} R_i^{\mathrm{T}} M_i^{-1} R_i$.

It can also be another iterative format. Starting with iterative Φ^k, we compute Φ^{k+1} as follows:

$$\Phi^{k+(i+1)/(p+1)} = \Phi^{k+i/(p+1)} + R_i^{\mathrm{T}} M_i^{-1} R_i (f - M\Phi^{k+i/(p+1)}), \quad i = 0, 1, \ldots, p \ (p = N)$$

ODDM is described in detail. Step 1: *Initialization*: Define sub-domains, overlapping regions, and maximum number of iterations.

Step 2: *Sub-region correction*: Update photon densities by using Equation (10) or Equation (11) at each sub-region.

Step 3: *Stopping condition*: Iterate coarse grid correction and sub-region correction until maximum number of iterations is reached or the difference between the newly updated and previous photon densities in the overlapping region is sufficiently small.

Step 4: *Boundary measurement data*: Computing $\partial\Omega$ by restricting photon densities of the detectors on the boundary.

DOI: 10.1002/cnm

3.3. Convergence analysis of Φ^k

We discuss the convergence of the iterative method equation (12), when M only is a symmetric positive definite Matrix, denoted as $M \succ O$. By $M \succcurlyeq O$ we denote a symmetric positive semi-definite matrix. The notation $M \succ N$ stands for $M - N \succ O$. Consider the solution of a linear system of n algebraic equation of the form $M\Phi = f$ in R^n by additive Schwarz iterations with overlapping blocks. The convergence of additive Schwarz iterations [15–18] is discussed now.

Definition 1 (*Horm and Johnson* [*15*])
Let M be a symmetric positive definite matrix, $\forall \boldsymbol{x} \in R^n$ be a column vector, then $\|x\|_M = (\boldsymbol{x}^{\mathrm{T}} M \boldsymbol{x})^{1/2}$ is weighted norm.

Definition 2 (*Horm and Johnson* [*15*])
Let M be a symmetric positive definite matrix, $\forall A \in R^{n \times n}$, then $\|A\|_M = [\mathrm{tr}(A^{\mathrm{T}} M A)]^{1/2}$ is defined as M-norm of matrix A.

Definition 3 (*Horm and Johnson* [*15*])
The spectral radius $\rho(B)$ for a matrix $B \in R^{n \times n}$ is $\rho(B) = \max\{|\lambda| : \lambda \in \lambda(B)\}$.

Definition 4 (*Frommer et al.* [*16*], *Frommer and Szyld* [*17*])
M splitting $M = B - C$ is called **P**-regular if $B^{\mathrm{T}} + C$ is a positive definite matrix.

Lemma 1 (*Frommer et al.* [*16*], *Frommer and Szyld* [*17*])
Let $M \succ O$, Then, $M = B - C$ is **P**-regular splitting if and only if $\|B^{-1}C\|_M < 1$.

Lemma 2 (*Frommer et al.* [*16*], *Frommer and Szyld* [*17*])
Given T_{as} from Equation (12), there is a pair of matrices A_{as} and B_{as} such that $M = A_{as} - B_{as}$. Matrix A_{as} is nonsingular and $T_{as} = A_{as}^{-1} B_{as}$.

Note: If $\lambda = 1$, in the absence of damping, we simply denote the matrix A_{as} as A, i.e. $A^{-1} = \sum_{i=1}^{p} R_i^{\mathrm{T}} M_i^{-1} R_i$.

Theorem 1
Let $M \succ O$ and let $M = A_{as} - B_{as}$ be the splitting defined in Lemma 1. If $\lambda < 1/p$, then this splitting is a **P**-regular splitting and therefore $\|T_{as}\|_M < 1$.

Proof
As pointed out above

$$A_{as}^{-1} = \lambda \sum_{i=1}^{p} R_i^{\mathrm{T}} M_i^{-1} R_i = \lambda \sum_{i=1}^{p} R_i^{\mathrm{T}} (R_i M R_i^{\mathrm{T}})^{-1} R_i = \lambda A^{-1} = \lambda p M^{-1}$$

then we can get $A_{as} = [1/(\lambda p)]M$; it is easy to see that $A_{as} \succ O$. $B_{as} = A_{as} - M = (1/\lambda)A - M = [1/(\lambda p) - 1]M$ is symmetric positive definite if $\lambda < 1/p$. Thus, $A_{as}^{\mathrm{T}} + B_{as} \succ O$, and the splitting is **P**-regular. By Lemma 2, we know $T_{as} = A_{as}^{-1} B_{as}$, which shows $\|T_{as}\|_M < 1$. □

Lemma 3 (*Horm and Johnson* [*15*])
Let $B \in R^{n \times n}$. We have

(1) If $\|\cdot\|$ be a matrix norm on $R^{n \times n}$, we have $\rho(B) \leqslant \|B\|$.
(2) For $\forall \varepsilon > 0$, there exists a norm $\|\cdot\|$ on $R^{n \times n}$, such that $\|B\| \leqslant \rho(B) + \varepsilon$.

Lemma 4
If $\|T_{as}\|_M < 1$, then $\rho(T_{as}) < 1$.

Proof
By Lemma 3, the proof is completed. □

Theorem 2
Let $T_{as} \in R^{n \times n}$, then $\lim_{k \to \infty} T_{as}^k = 0$ if and only if $\rho(T_{as}) < 1$.

DOI: 10.1002/cnm

Proof
If $\lim_{k\to\infty} T_{as}^k = 0$, we assume $\lambda \in \lambda(T_{as})$ and $\rho(T_{as}) = |\lambda|$. For an $\forall k$ such that $\lambda^k \in \lambda(T_{as}^k)$, by Lemma 3, we have $\rho(T_{as})^k = |\lambda|^k \leqslant \rho(T_{as}^k) \leqslant \|T_{as}^k\|_M$. For all k, it shows $\rho(T_{as}) < 1$. Conversely, if $\rho(T_{as}) < 1$, by using Lemma 3 and Theorem 1, there exists a norm $\|\cdot\|$, such that $\|T_{as}\| < 1$. It shows $0 \leqslant \|T_{as}^k\| \leqslant \|T_{as}\|^k \to 0,\ k \to \infty$, which means $\lim_{k\to\infty} T_{as}^k = 0$. □

If the iterative method equation (12) is convergence, we assume that its limit is Φ^*. Then, we have

$$\Phi^* = T_{as}\Phi^* + A_{as}^{-1} f \tag{13}$$

which means that Φ^* is the solution of Equation (13).

Combining Equations (12) and (13), we have

$$\Phi^{k+1} - \Phi^* = T_{as}(\Phi^k - \Phi^*), \quad k = 0, 1, 2, \ldots \tag{14}$$

We can derive $\Phi^k - \Phi^* = T_{as}^k(\Phi^0 - \Phi^*)$ from Equation (14). Giving any initial value Φ^0, by Theorem 2, the sequence $\{\Phi^k\}$ converges to Φ^* if and only if $T_{as}^k \to 0$ as $k \to \infty$. It is so obvious that we have got our conclusion. □

3.4. Source reconstruction for inverse problem

In Equation (1), when photon flux density Φ is obtained by ODDM, how to reconstruct source $S(x)$?

Let $\{r_1, r_2, \ldots, r_{Ns_k}\}$ be the interpolation basis function, and $S(x)$ is approximated by

$$S_k(x) = \sum_{i=1}^{N_{s_k}} s_i(x) r_i(x)$$

where N_{s_k} and $s_i(x)$ are the values of the interpolation basis function and the interpolation nodal values, respectively. The selection of interpolation basis function r_i may be the same as or different from that of the nodal basis function ψ_i, which depends on the choice of source variables s_i. We select the basis source variable and piecewise constant function as the interpolation basis function, which are different from the piecewise linear nodal basis function ψ_i. We have

$$S_k(x) = \sum_{i=1}^{N_k} \alpha(\psi_i, \psi_j)\Phi_j = f(\psi_j), \quad j = 1, 2, \ldots, N_k$$

The matrix form of Equation (2) can be obtained as follows:

$$M\Phi = F^* S \tag{15}$$

where

$$M = \begin{pmatrix} \alpha(\psi_1, \psi_1) & \cdots & \alpha(\psi_{N_k}, \psi_1) \\ \vdots & \ddots & \vdots \\ \alpha(\psi_1, \psi_{N_k}) & \cdots & \alpha(\psi_{N_k}, \psi_{N_k}) \end{pmatrix}, \quad \Phi = \begin{pmatrix} \Phi_1 \\ \vdots \\ \Phi_{N_k} \end{pmatrix}$$

$$F^* = \begin{pmatrix} \int_{\Omega_k} r_1\psi_1 \,\mathrm{d}x & \cdots & \int_{\Omega_k} r_{N_k}\psi_1 \,\mathrm{d}x \\ \vdots & \ddots & \vdots \\ \int_{\Omega_k} r_1\psi_{N_k} \,\mathrm{d}x & \cdots & \int_{\Omega_k} r_{N_k}\psi_{N_k} \,\mathrm{d}x \end{pmatrix}, \quad S = \begin{pmatrix} S_1 \\ \vdots \\ S_{N_k} \end{pmatrix}$$

DOI: 10.1002/cnm

For a brief description of the reconstruction method, we rearrange Equation (15) as follows:

$$\begin{pmatrix} M_{11} & M_{12} \\ M_{12}^{\mathrm{T}} & M_{22} \end{pmatrix} \begin{pmatrix} \Phi^m \\ \Phi^* \end{pmatrix} = \begin{pmatrix} F_{11} & F_{12} \\ F_{21} & F_{22} \end{pmatrix} \begin{pmatrix} S^p \\ S^* \end{pmatrix} \tag{16}$$

where Φ^m represents the nodal flux density on the boundary $\partial\Omega$, which is computed from the surface flux image captured with a charge coupled device (CCD) camera, and the flux density on the internal nodes is denoted as Φ^*. The unknown source intensities in the region where reporter genes are tagged are S^p and S^*; the latter is equal to zero since no emission source exists in that region. It is noted that the region for S^p is larger than the exact region where the reporter genes are present. Thus, Equation (15) is reduced to

$$A_k S^p = \Phi^m \tag{17}$$

where $A_k = (M_{11} - M_{12}M_{22}^{-1}M_{12}^{\mathrm{T}})^{-1}(F_{11} - M_{12}M_{22}^{-1}F_{21})$. The reconstruction of the light source distribution can be expressed as a non-negative vector $\{S^p\}$, which optimally minimizes the difference between the computed surface nodal flux density Φ^m via Equation (16), and the computed Φ^m, which is obtained from the forward model as the experimental data on the surface which is

$$\Theta_k(S^p) = \min_{0 \leqslant S^p \leqslant S_{\mathrm{sup}}^k} \{\|AS^p - \Phi^m\|_\Lambda + \theta\eta_k(S^p)\} \tag{18}$$

where S_{sup}^k is the upper bound of source density, Λ is the weight matrix in $\|V\|_\Lambda = V^{\mathrm{T}}\Lambda V$, θ is the regularization parameter and $\eta_k(S_k^p)$ is the penalty function. Because the genetic algorithm [19–21] has global convergence, we adopt it to solve Equation (18).

4. NUMERICAL SIMULATIONS

A series of computational experiments are designed by ODDM. We compare ODDM and FEM. Two kinds of model (sphere and cylinder) are applied in Sections 4.1 and 4.2. Optical parameters from [4] are listed in Table I.

4.1. Forward problem for two different tissue sphere phantom models

BLT forward problem is to find the photon flux density in the biological tissue and the outgoing flux on its boundary.

Consider a uniform spherical light source with radius r_0 and total power s, centering at x_0 in a homogeneous medium. The photon flux density Φ at point x in the medium is

$$\Phi(x) = \frac{\exp(-\mu_{\mathrm{eff}} r)}{r D(\mu_{\mathrm{eff}})^2} \left(r_0 \cosh(\mu_{\mathrm{eff}} r_0) - \frac{1}{\mu_{\mathrm{eff}}} \sinh(\mu_{\mathrm{eff}} r_0) \right)$$

where $r = \|x - x_0\|$ and μ_{eff} denotes the effective attenuation coefficient

$$\mu_{\mathrm{eff}} = (\mu_a / D)^{1/2} = (3\mu_a(\mu_a + \mu_s(1-g)))^{1/2}$$

as shown in Figure 2(a), a finite element volume mesh was made. The solid spherical source of radius 0.5 mm and flux 1 W was located at the center, as shown in Figure 2(b). The spherical models were designed to have various radii ranging from 1 to 10 mm.

Table I. Optical parameters of the heterogeneous phantom.

Material	$\mu_a(\mathrm{mm}^{-1})$	$\mu_s(\mathrm{mm}^{-1})$	g
Lung (Lu)	0.35	23	0.94
Heart (H)	0.2	16.0	0.85

DOI: 10.1002/cnm

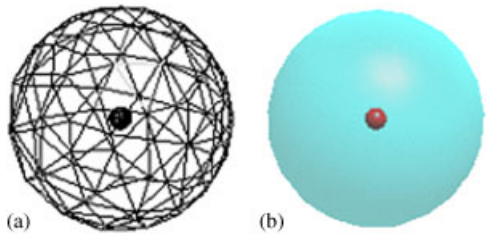

Figure 2. Finite-element meshes for modeling ideal source and detection spheres: (a) detection sphere and (b) solid spherical source at the center of the detection sphere.

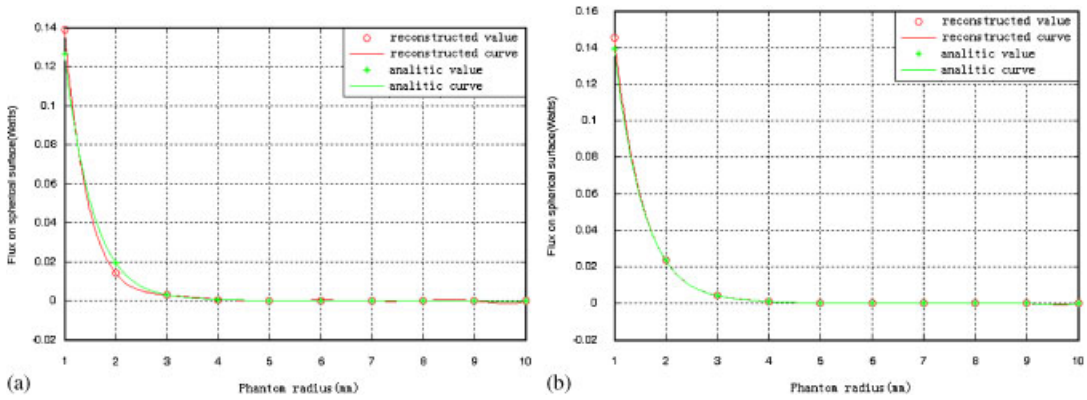

Figure 3. Comparison between the ODDM solution and the analytic solution for two kinds of optical parameter: (a) $\mu_s = 23\,\mathrm{mm}^{-1}$, $\eta_a = 0.35\,\mathrm{mm}^{-1}$, $g = 0.94$ and (b) $\mu_s = 16\,\mathrm{mm}^{-1}$, $\eta_a = 0.2\,\mathrm{mm}^{-1}$, $g = 0.85$.

We compare between the total flux photon density by the ODDM and the analytical solution based on the two different tissue models (see below Figure 3).

As shown in Figure 3, the solution of the described ODDM is identical to the analytical solution as well. It is observed that flux decreases with the increment of the sphere radius at different rates. Since the photon takes a longer total optical path to reach the spherical surface, the larger radius and the stronger the absorption, the weaker the signal on the surface. The variation of the falling rate of the flux in different tissue models is attributed to complex scattering and absorption processes in the medium.

4.2. Inverse problem for cylinder phantom model

A cylindrical phantom 30 mm in height and 10 mm radius is divided into tetrahedral 288 elements and 124 nodes, as shown in Figure 4. The phantom was homogenized with optical parameters $\mu_s = 23\,\mathrm{mm}^{-1}$, $\mu_a = 0.35\,\mathrm{mm}^{-1}$, $g = 0.94$ and $n = 1.37$. We assumed that a solid spherical source of 1 mm diameter having the power of 1 W is put at (−0.323096, 0.263254, 0.42990) inside the cylindrical phantom. It includes 22 node numbers and each has the power of 0.0455 W. Based on this model, the source reconstruction was carried out by using ODDM. The relative error (re) between the real and reconstructed source energy is defined by

$$\mathrm{re} = \frac{\|\text{reconstucted flux} - \text{exact flux}\|}{\text{exact flux}}$$

In this experiment the photon flux density Φ is obtained by ODDM. The advantages of ODDM are demonstrated as follows:

First, the flux error distribution for reconstructed source is drawn up. As shown in Figure 5, there is an excellent agreement between the real and reconstructed source energy. The relative errors of the bulk source intensities are 0.35997, 0.23267, 0.30891 and 0.01202 when 0, 2, 4 and

DOI: 10.1002/cnm

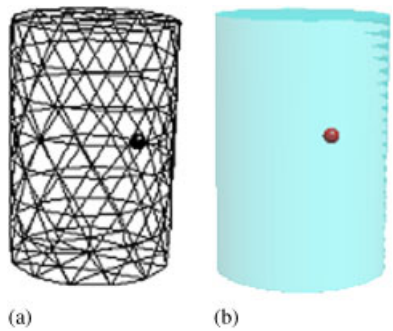

Figure 4. Finite-element meshes for modeling a homogeneous cylindrical body and a solid spherical source: (a) cylindrical body of homogeneous optical properties and (b) solid spherical source at the center of the cylindrical body.

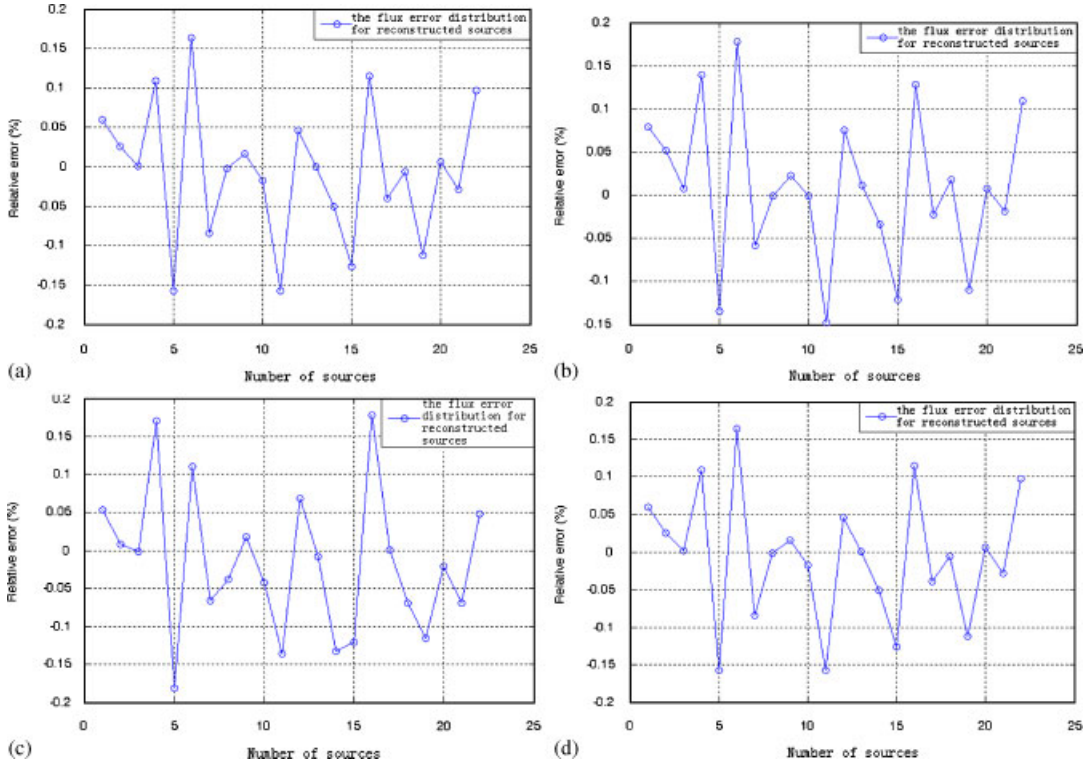

Figure 5. Relative errors in terms of source intensity with (a) 0%; (b) 2%; (c) 4%; and (d) 6% noise added to the flux data measured on the surface of the cylindrical tissue phantom.

6% random noise are respectively added to the data measured on the surface of the cylindrical phantom.

Second, the actual reconstructed source centers and energy density for different regularization parameter θ is given in Table II. Here, we assume a solid spherical source of 1 mm diameter having the power of 1 W was put at (−0.323096, 0.263254, 0.42990). The convergence condition is that the total of the source density is between 0.3 and 1. θ must be between 0.0006 and 0.00001, or else, it cannot satisfy the convergent condition. It is easy to see that when $\theta = 0.0008$, it gives the best reconstructed position, but has higher relative error.

Finally, the reconstructed results by FEM and ODDM, respectively, are compared. Table III lists the numerical results.

DOI: 10.1002/cnm

Table II. Comparison between the actual reconstructed source centers and energy density for different regularization parameter θ and initial value.

θ	Recons. pos	Recons. density (W)	re
0.0007	(0.110475, 0.993879, 0.436038)	0.393	0.607
0.0008	(−0.976364, 0.216131, 0.415819)	0.337	0.663
0.0009	(−0.166014, 0.986123, 0.876151)	0.359	0.641

Table III. Comparison with FEM.

	θ	Recons. Pos	Density (W)	re
FEM	0.0007	(−0.166, 0.986, 0.876)	0.201	0.799
	0.0008	(−0.976, 0.216, 0.415)	0.067	0.933
ODDM	0.0007	(0.110, 0.994, 0.436)	0.393	0.607
	0.0008	(−0.976, 0.216, 0.415)	0.337	0.663

Obviously for same θ, ODDM has higher energy density and lower relative error than FEM. Hence, ODDM is an effective method for BLT.

5. CONCLUSIONS

Domain decomposition methods are applied widely [22–25] ODDM refers to divide and conquer techniques for solving partial different equations by iteratively defining sub-problems on smaller sub-domains. It can handle complex and irregular geometries, singularities and anomalous regions. We have developed a reconstruction algorithm to identify a 3D bioluminescent source distribution by incorporating *a priori* knowledge, which is important and helpful to identify the source region. The more *a priori* information we have, the more precise and stable BLT reconstruction becomes. The simulation experiments have shown that ODDM is computationally efficient and fairly robust with respect to initial distribution and permissible region size, but it is important for us to choose an initial value for ODDM. Our future work will focus on light source reconstruction using the parallel method.

ACKNOWLEDGEMENTS

This work is supported by Chair Professors of Cheung Kong Scholars Programme, the Program for Cheung Kong Scholars, Innovative Research Team in University (PCSIRT, IRT0645), National Basic Research Program of China (NBRPC, 2006CB705700) and Shaanxi Science and Technology Programming (2007K08-06).

REFERENCES

1. Ntziachristos V, Ripoll J, Wang LV, Weissleder R. Looking and listening to light: the evolution of whole-body photonic imaging. *Nature Biotechnology* 2005; **23**:313–320.
2. Wang G, Li Y, Jiang M. Uniqueness theorems in bioluminescence tomography. *Medical Physics* 2004; **31**: 2289–2299.
3. Li H, Tian J, Zhu F, Cong W, Wang LV, Hoffman EA, Wang G. A mouse optical simulation environment (MOSE) to investigate bioluminescent phenomena in the living mouse with the Monte Carlo method. *Academic Radiology* 2004; **11**:1029–1038.
4. Wang G, Hoffman EA, McLennan G, Wang LV, Suter M, Meinel JF. Development of the first bioluminescent CT scanner. *Radiology* 2003; **229**:566.
5. Cong W, Wang G, Kumar D, Liu Y, Jiang M, Wang LV, Hoffman EA, McLennan G, McCray PB, Zabner J, Cong A. Practical reconstruction methods for bioluminescence tomography. *Optics Express* 2005; **13**:6756–6771.
6. Cong W, Kumar D, Liu Y, Cong A, Wang G. A practical method to determine the light source distribution in bioluminescent imaging. *Proceedings of the SPIE*, Denver, CO, U.S.A., vol. 5535, 2004; 679–686.

DOI: 10.1002/cnm

7. Lv YJ, Tian J, Cong W, Wang G, Luo J, Yang W, Li H. A multilevel adaptive finite element algorithm for bioluminescence tomography. *Optics Express* 2006; **14**:8211–8223.
8. Schweiger M, Arridge SR, Hiraoka M, Delpy DT. The finite element approach for the propagation of light in scattering media: boundary and source condition. *Medical Physics* 1995; **22**:1779–1792.
9. Tai X-C. Rate of convergence for some constraint decomposition methods for nonlinear variational inequalities. *Numerische Mathematik* 2003; **93**(4):755–786.
10. Jiang M, Wang G. Image reconstruction for bioluminescence tomography. *Proceedings of the SPIE*, Denver, CO, U.S.A., vol. 5535, 2004; 335–351.
11. Wang G, Jiang M, Tian J, Cong W, Li Y, Han W, Kumar D, Qian X, Shen H, Zhou T, Cheng J, Lv Y, Li H, Luo J. Recent development in bioluminescence tomography. *Presented in the Third IEEE International Symposium on Biomedical Imaging* (*ISBI 2006*), *VA*, *U.S.A.*, 6–9 April 2006.
12. Nabben R. Comparisons between multiplicative and additive Schwarz iterations in domain decomposition methods. *Numerische Mathematik* 2003; **95**:145–162.
13. Chan TF, Mathew TP. Domain decomposition algorithms. *Acta Numerica* 1994; **3**:61–143.
14. Xu J. Iterative methods by space decomposition and subspace correction. *SIAM Review* 1992; **34**:581–613.
15. Horm RA, Johnson CR. *Matrix Analysis*. Post & Telecom Press: Beijing, China, 1986; 257–335.
16. Frommer A, Nabben R, Szyld DB. Weighted max norms, splittings, and overlapping additive Schwarz iterations. *Numerische Mathematik* 1999; **83**:259–278.
17. Frommer A, Szyld DB. An algebraic convergence theory for restricted additive Schwarz methods using weighted max norm. *SIAM Journal on Numerical Analysis* 2001; **39**:463–479.
18. Marec I, Szyld DB. *Algebraic Analysis of Schwarz Methods for Singular Systems*. Lecture Notes in Computational Science and Engineering, vol. 40. Springer: Berlin, 2005; **40**:647–652.
19. Fang W, Wu T, Chen P. An algorithm global optimization for rational functions with rational constraints. *Journal of Global Optimization* 2000; **18**:211–218.
20. Lim MH, Yuan Y, Omatu S. Efficient genetic algorithms using simple genes exchange local search policy for the quadratic assignment problem. *Computational Optimization and Applications* 2000; **15**:249–268.
21. Chattopadhyay S, Choudhary N. Genetic algorithm based approach for low power combinational circuit testing. *Proceedings of the 16th International Conference on VLSI Design* (*VLS' 3*). IEEE Computer Society: Washington, DC, 2003.
22. Dryja M, Widlund OB. *Towards a Unified Theory of Domain Decomposition Algorithms for Elliptic Problems, Iterative Methods for Large Systems*. Academic Press: New York, 1990.
23. Kwon K, Son I, Yazici B. Domain decomposition method for diffuse optical tomography. *Computational Imaging III* 2005; **5674**:64–75.
24. Du Q, Yu D. A domain decomposition method based on natural boundary reduction for nonlinear time-dependent exterior wave problems. *Neural Computing and Applications* 2002; **68**:111–129.
25. Nabben R, Vuik C. Domain decomposition methods and deflated Krylov subspace iterations. *European Conference on Computational Fluid Dynamics*, Egmond aan Zee, The Netherlands, 2006.

DOI: 10.1002/cnm